The role of Cu on the reduction behavior and surface properties of Fe-based Fischer–Tropsch catalysts†

Emiel de Smit,[a] Frank M. F. de Groot,[a] Raoul Blume,[b] Michael Hävecker,[b] Axel Knop-Gericke[b] and Bert M. Weckhuysen*[a]

Received 29th September 2009, Accepted 2nd November 2009
First published as an Advance Article on the web 19th November 2009
DOI: 10.1039/b920256k

The effect of Cu on the reduction behavior and surface properties of supported and unsupported Fe-based Fischer–Tropsch synthesis (FTS) catalysts was investigated using *in situ* X-ray photoelectron spectroscopy (XPS) and *in situ* X-ray absorption spectroscopy (XAS) in combination with *ex situ* bulk characterization. During exposure to 0.4 mbar $CO–H_2$ above 180 °C, the reduction of CuO to Cu^0 marked the onset of the reduction of Fe_3O_4 to α-Fe. The promotion effects of Cu are explained by a combination of spillover of H_2 and/or CO molecules from metallic Cu^0 nuclei to closely associated iron oxide species and textural promotion. XAS showed that in the supported catalyst, Cu^+ and Fe^{2+} species were stabilized by SiO_2 and, as a result, Fe species were not reduced significantly beyond Fe_3O_4 and Fe^{2+}, even after treatment at 350 °C. After the reduction treatment, XPS showed that the concentration of oxygen and carbon surface species was higher in the presence of Cu. Furthermore, it was observed that the unsupported, Cu-containing catalyst showed higher CO_2 concentration in the product gas stream during and after reduction and Fe surface species were slightly oxidized after prolonged exposure to $CO–H_2$. These observations suggest that, in addition to facilitating the reduction of the iron oxide phase, Cu also plays a direct role in altering the surface chemistry of Fe-based FTS catalysts.

1. Introduction

In Fischer–Tropsch synthesis (FTS), synthesis gas ($CO + H_2$) is converted into longer hydrocarbon chains through a surface polymerization reaction.[1–3] Recently, there has been a renewed interest in FTS as it presents an attractive way to produce chemicals and transportation fuels from carbon sources alternative to crude oil. FTS is catalyzed by all first row group VIII transition metals and Ru, although Co and Fe have the most desirable catalytic and economic properties.[4] Fe-based catalysts are applied in both high temperature FTS (280–350 °C, HTFT), mainly aimed at the production of short-chain olefins, and low temperature FTS (200–250 °C, LTFT) yielding long chain hydrocarbons and waxes as main products. The Fe-based FTS catalysts also catalyze the water-gas shift reaction (WGS) under typical reaction conditions and therefore these materials are of prime interest for the conversion of hydrogen lean ($CO/H_2 \approx 1$) synthesis gas types, like those derived from coal and biomass.[5] Both carbon sources are expected to play a large role in future FTS applications.

Although the exact nature of the active site in Fe-based FTS catalysts is still the subject of debate, it is clear that the iron oxide catalyst precursors need to be reduced to zero-valent Fe (*i.e.* metallic or carbidic) before they are active in FTS.[3,6] The use of Cu as a promoter has been first reported in early catalyst formulation patents, claiming higher FTS rates even at Cu contents below 2 wt%. Since then, Cu has been a commonly added promoter in Fe-based FTS catalysts, facilitating the reduction of the Fe^{3+} iron oxide (α-Fe_2O_3, α-FeOOH) precursor to zero-valent Fe during the activation of the catalyst in H_2, CO or synthesis gas.[7–20] The moderate temperatures that are needed to reduce Cu-containing catalysts prevent sintering (the loss of catalytically active surface area), a phenomenon prevalent at higher reduction temperatures, of the active zero-valent Fe phase. Consequently, Cu-containing catalysts show superior FTS activity compared to unpromoted catalysts. Furthermore, it is reported that Cu increases the FTS selectivity towards longer hydrocarbon chains and the paraffin to olefin ratio[11,13,15,16,18] as well as the WGS activity.[11,13,16,19]

Apart from detailed studies on the effects of the Cu promoter on the catalyst reduction and FTS properties, the exact role and physicochemical state of the Cu species

[a] *Inorganic Chemistry and Catalysis group, Debye Institute for Nanomaterials Science, Utrecht University, Sorbonnelaan 16, 3584 CA Utrecht, The Netherlands. E-mail: b.m.weckhuysen@uu.nl; Fax: +31 30 251 1027; Tel: +31 30 253 7400*
[b] *Fritz-Haber-Institut der Max-Planck-Gesellschaft, Department of Inorganic Chemistry, Faradayweg 4-6, 14195 Berlin, Germany. E-mail: knop@fhi-berlin.mpg.de; Fax: +49 30 8413 4690; Tel: +49 30 8413 4422*

† Electronic supplementary information (ESI) available: Transmission electron microscopy images of the catalysts after calcination and after treatment in 0.4 mbar $CO–H_2$; O K-edge XAS spectra of the catalysts before reduction treatment; Fe L-edge XAS spectra of the unsupported catalysts after treatment in 0.4 mbar $CO–H_2$; mass spectrometry data acquired during treatment in 0.4 mbar $CO–H_2$; O K-edge XAS spectra of the catalysts after treatment in 0.4 mbar $CO–H_2$; Cu XPS spectrum of the Fe_2O_3–Cu catalyst after treatment in 0.4 mbar $CO–H_2$; O 1s XPS spectra of the catalysts during treatment in 0.4 mbar $CO–H_2$. For ESI see DOI: 10.1039/b920256k

in promoted catalysts have rarely been studied directly. Wielers *et al.*[12,13] investigated silica supported bimetallic Fe–Cu catalysts using Mössbauer and IR spectroscopy. The group reported that the Cu phase facilitated the reduction of Fe^{3+} species into Fe^{2+} (iron(II) silicate) species and, subsequently to zero-valent Fe. The zero-valent Fe was present as monometallic Fe particles as well as bimetallic Fe–Cu entities. Furthermore, the group could distinguish CO bonded to Cu and Fe using IR spectroscopy, and used this to characterize the surface of the catalyst. It was observed that prolonged exposure of the materials to CO led to an Fe enrichment of the surface which the authors attributed to the differences between the heat of adsorption between Cu and Fe[21] (-63 kJ mol^{-1} and -167 kJ mol^{-1}, respectively). Unfortunately, the lowest Cu concentration in the reported samples was 80/20 Fe/Cu at./at., well above the typically added amounts in FTS catalysts. In an X-ray photoelectron spectroscopy (XPS) study, Wachs *et al.*[10] characterized the surface of a pre-reduced, passivated FTS catalyst after *in situ* re-activation in H_2 at 350 °C and 16 h FTS. Their impregnated catalyst contained 1.4 wt% Cu. The group observed agglomeration of the Cu phase on the surface of the reduced catalysts (*i.e.* decreasing Cu/Fe ratios). However, apart from the facilitation of the reduction of the passivated catalyst, no significant differences were found in FTS performance and carburization rate of the catalyst compared to an unpromoted Fe catalyst.

Zhang *et al.*[18] used IR spectroscopy to probe the surface basicity of their Fe–Mn–Cu/SiO_2 catalyst, but observed no significant differences between Cu-promoted and unpromoted catalysts.

Our previous work dealt with the characterization of the local and long-range (bulk) structure of Cu-promoted FTS catalysts by combined X-ray absorption fine structure spectroscopy (XAFS) and wide angle X-ray scattering (WAXS) techniques.[20] Here it was shown that Cu significantly increased the reduction rate of the catalysts to zero-valent Fe species and increased the FTS activity and selectivity toward longer hydrocarbon products. Furthermore, it was observed that the Cu-promoted catalysts preferentially formed θ-Fe_3C crystallites, while the unpromoted catalyst mainly converted to ε-Fe_2C/ε′-$Fe_{2.2}C$ crystallites during FTS. In two other related studies we obtained a closer look of a working Cu-containing Fe-based FTS catalyst particle during activation in H_2[22] and CO hydrogenation[23] using *in situ* scanning transmission X-ray microscopy (STXM). The technique relies on a focused soft X-ray beam (~200–2000 eV) to characterize materials at a ~25 nm resolution using X-ray absorption spectroscopy (XAS). Using both techniques, however, it was not possible to directly study the Cu phase during reduction or FTS. Also, while in principle bulk characterization can prove very useful in structure–activity correlations, the surface structure is crucial for catalytic activity and therefore key in understanding reduction and other reaction phenomena.

A recently developed, powerful technique for studying the (sub-)surface of catalysts is synchrotron-based high pressure XPS. The technique relies on differential pumping in order to enable the detection of XPS spectra in the presence of reactant gases. Currently, the technique is limited to the mbar range. However, studying a catalyst surface *in situ*, *i.e.* in the presence of reactant gases and at elevated pressures, is an important step towards closing the so-called 'pressure gap' between surface science and 'real' heterogeneous catalysis, and can be used to obtain important new insights into catalyst systems.[24,25] The use of a synchrotron radiation source for XPS has some additional important advantages over traditional laboratory X-ray sources. Since the energy of the incident X-ray light is tunable, the kinetic energies of the electrons escaping from the surface of the catalyst can be tuned. By studying electrons of the same kinetic energy, one can obtain more detailed information of the surface and subsurface of catalytic materials and use this to probe the surface at different depths.

In the present study, we have used synchrotron-based *in situ* XPS and XAS in the soft X-ray range to study the surface of Cu-promoted Fe-based FTS catalysts. The bulk properties of the materials were further characterized *ex situ*, using X-ray fluorescence analysis (XRF), N_2-physisorption, transmission electron microscopy (TEM), temperature programmed reduction (TPR) and X-ray diffraction (XRD). Based on these results, the various roles of Cu as promoter element in Fe-based FTS catalysis are discussed.

2. Experimental method

2.1 Catalyst preparation

An unpromoted Fe (denoted as Fe_2O_3) and singly promoted Fe/Cu (denoted as Fe_2O_3–Cu) catalyst, as well as a more complex, fully promoted Fe/Cu/K/Si (denoted as Fe_2O_3–Cu–K–Si) catalyst were prepared by precipitating a ferric nitrate solution in a basic sodium carbonate solution.[9] The detailed preparation method of the materials is described elsewhere.[20] In short, $Fe(NO_3)_3{\cdot}9H_2O$ (Acros, 98 + %) and, where applicable, $Cu(NO_3)_2{\cdot}3H_2O$ (Merck, p.a. 99,5%) were added to a near boiling Na_2CO_3 solution under vigorous stirring. The resulting precipitate was re-slurried and washed several times in order to remove any residual sodium. For the Fe_2O_3–Cu–K–Si catalyst material, a potassium waterglass solution (K_2O : SiO_2 (1 : 2.15), Akzo-PQ) was added to the Fe- and Cu-containing slurry under vigorous stirring. All samples were dried at 120 °C for 24 h and subsequently calcined at 300 °C for 3 h.

2.2 Bulk characterization methods

The final catalyst precursor compositions were confirmed by X-ray fluorescence (XRF) analysis on a Goffin Meyvis Spectro X-lab 2000 machine. The BET surface area and total pore volume of the catalysts were determined from N_2-physisorption. N_2-physisorption isotherms were measured at -196 °C using a Micromeritics Tristar 3000 apparatus. The samples were dried in He flow for 14 h at 200 °C (5 °C min^{-1} ramp) prior to analysis. The catalysts were also analyzed before reduction and after the *in situ* XPS/XAS experiments using transmission electron microscopy (TEM) in a Tecnai 20F FEG microscope operating at 200 kV and equipped with energy dispersive X-ray (EDX) and selected area diffraction (SAD) analyzers allowing us to obtain information about the crystallinity and distribution of chemical species on the materials under study.

Temperature programmed reduction (TPR) experiments were performed using a Micromeritics Autochem-II instrument equipped with a TCD detector. The samples were initially dried in an Ar flow at 120 °C for 20 min and after the TCD signal was stable, the gas stream was switched to 5% H_2–Ar gas mixture (50 mL min^{-1}) and the H_2 consumption was measured. The temperature was raised from 50 to 800 °C at a rate of 5 °C min^{-1} and held at that temperature for 1 h. X-Ray diffraction (XRD) powder patterns of the catalysts before reduction and after the *in situ* XPS/XAS experiments were acquired on a Bruker D8 X-ray powder diffraction instrument using CoKα radiation (1.7902 Å). The line broadening of the α-Fe_2O_3 (*h k l* = 1 0 4) diffraction peak at 38.7° 2θ and the (*h k l* = 1 1 0) α-Fe diffraction peak at 52.4° 2θ was used to estimate the relevant crystallite sizes.

2.3 Surface characterization methods

The reduction of the catalysts was studied *in situ* using X-ray absorption spectroscopy (XAS) and X-ray photoelectron spectroscopy (XPS). The reduction of iron oxide to metallic Fe is in principle endergonic, but thermodynamically feasible at low enough partial pressures of H_2O.[26,27] In our work, it was found that the materials could not be fully reduced in ~1 mbar H_2. Reduction of iron oxides in CO is exergonic. However, at 1 mbar CO, our catalysts could also not be completely reduced and therefore the reduction experiments were carried out using a mixture of CO–H_2. Experiments were performed at the ISISS-PGM beamline at the Berliner Synchrotron Radiation Facility (BESSY) in Berlin (Germany). The experimental setup and principles for measuring *in situ* XPS and XAS are described in more detail elsewhere.[24,28–30] In brief, the samples were pressed into a self-supporting wafer (~20 mg) and mounted on a sapphire sample holder, 2 mm away from a 1 mm diameter aperture to a differentially pumped electrostatic lens system. Photoelectrons created at the sample travel through the lens system and are analyzed on a Phoibos 150 hemispherical analyzer (SPECS GmbH, Berlin, Germany). The application of differential pumping in combination with the electrostatic lenses allows the collection of photoelectrons with an efficiency similar to that of a conventional hemispherical analyzer. XAS measurements at the Fe L_3 and L_2, Cu L_3 and L_2 and O K absorption edges were carried out *in situ* by using total gas phase conversion electron yield (CEY) detection.[29] The resolution of the XAS measurements was ~0.1 eV at the O K-edge. Sample heating was realized by using an infrared laser system, aimed at the backside of the sample, in combination with temperature feedback control through a thermocouple fitted on the front side of the sample. Gas flows through the reaction cell were regulated through mass flow controllers. Gas phase reactants and products were analyzed by a mass spectrometer connected to the outlet of the reaction chamber.

The combined CO and H_2 pressure in the experimental cell was 0.4 mbar at a total flow rate of 10 mL min^{-1}. The CO/H_2 ratio was kept at 2 for all experiments. Samples were heated to 180 °C in H_2 flow (0.4 mbar) before exposure to the CO–H_2 mixture. This was done (1) to prevent the formation of gas phase carbonyls and (2) to prevent excessive sample charging in the X-ray beam, interfering with the XPS analysis. Concerning the latter point, it was observed that after mild reduction in H_2 at 180 °C the sample became conductive (due to the formation of Fe_3O_4) and no charging was observed.

The surface of the Fe_2O_3 and Fe_2O_3–Cu samples was analyzed by XPS after reaching 275 °C in CO–H_2, after 0.5 h at 275 °C, after 1 h at 275 °C and after evacuating the reaction chamber. The Fe_2O_3–Cu–K–Si sample was characterized after reaching 275 °C, after 1 h at 275 °C, and after 1 h at 350 °C. The Fe($2p_{3/2}$, $2p_{1/2}$), Cu($2p_{3/2}$, $2p_{1/2}$), O(1s), C(1s), K($2p_{3/2}$, $2p_{1/2}$) and Si($2p_{3/2}$) spectral lines were probed using 1200, 1050 and 850 eV incident X-ray energy. The inelastic mean free paths (IMFP) of the photoelectrons resulting from each incident energy were calculated at each temperature step using the TPP2M formula,[31] and assuming a near-surface catalyst composition based on the *in situ* XAS experiments at that specific temperature (either pure Fe^0 or Fe_3O_4). The reported XPS peak positions were calibrated with respect to the valence band or Cu(2p) (932.7 eV) and O(1s) (532.0 eV) XPS binding energies. The surface sensitivity of XPS data is reported in terms of the inelastic mean free path (IMFP) λ of the created photoelectrons. In our experiment geometry (normal takeoff angle), 65% of the photoelectrons originate from within λ.

Atomic ratios were compared at same sampling depths by calculating and comparing XPS signals coming from electrons of similar kinetic energy, and thus a similar IMFP in the solid. Atomic sensitivity factors (ASF) were taken into account for the determinations of the atomic ratios and calculated using:

$$\mathrm{ASF} = B \times \sigma \times \lambda_{\mathrm{tot}} \times T \qquad (1)$$

where B is the instrumental contribution factor, σ is the ionization cross-section for a given photon energy,[32] λ_{tot} is the total escape depth[33] and T is the transmission through the surface, which was assumed to be unity. B is assumed to be the same for all atoms and therefore can be disregarded. The XPS peak areas were determined by using the background subtraction method as recommended by Shirley.[34] Finally, the XPS peak areas were normalized to the total flux of X-ray light at the sample, taking into account the BESSY storage ring current and monochromator efficiency.

The inherent surface sensitivity of the photoelectrons created in XPS and the somewhat less surface sensitive (about ~4 nm in our experiment) conversion electron yield (CEY) detection used in XAS, in combination with the *ex situ* bulk characterization by XRD, provided detailed information from the sample from different sampling depths.

3. Results and discussion

Before and after the *in situ* XAS and XPS experiments, the composition, structure and texture of the catalysts was characterized *ex situ* using XRF, N_2-physisorption, TEM, H_2 TPR and XRD. These results will be considered first and will be used as a reference for the bulk structure of the catalysts. The subsequently presented *in situ* XPS and XAS results will be used to discuss the changes in surface and near-surface structure of the catalysts during treatment in CO–H_2.

3.1 Bulk catalyst composition, structure and texture

Table 1 summarizes the catalyst composition as measured from XRF, along with the BET surface area and total pore volume of the materials under study before and after treatment in 0.4 mbar CO–H_2.

From the table it is clear that the addition of a relatively small amount of SiO_2 has a dramatic effect on the precursor specific surface area and pore structure. After treatment in 0.4 mbar CO–H_2, the surface area of the unsupported Fe_2O_3 and Fe_2O_3–Cu catalyst decreased dramatically. Moreover, the porosity of the catalysts is strongly affected, with the pore structure collapsing after treatment. Strikingly, the supported Fe_2O_3–Cu–K–Si catalyst also shows a dramatic loss of surface area and pore volume.

Fig. 1 shows the reduction profiles of the three catalyst precursors (normalized per mol Fe) during reduction in H_2, as determined from TPR. All reduction profiles show the expected two step reduction process of α-Fe_2O_3 to α-Fe.[26,35,36]

The CuO present in the promoted samples contributes to the consumption of H_2. However, because of the strong influence of CuO morphology on the observed T_{max} values in TPR experiments,[37] and the overlap of Fe and Cu reduction peaks, it was not possible to reliably estimate the contribution of the CuO species to the H_2 uptake by deconvolution of the TPR peaks. Therefore, this contribution will be discussed on the basis of the expected consumption of H_2 by CuO species as calculated from the molar composition from XRF analysis and assuming the uptake of one mol H_2 per mol CuO.

A clear shift in the onset of the first reduction step is observed in the Cu-promoted catalysts. While the unpromoted catalyst shows two peaks (T_{max} = 290 and 377), the promoted catalysts show one major contribution, with T_{max} at 220 °C and 283 °C for the Fe_2O_3–Cu sample and Fe_2O_3–Cu–K–Si, respectively. This peak is ascribed to the reduction step of Fe^{3+} in α-Fe_2O_3 to Fe^{2+} in the mixed $Fe^{2+/3+}$ inverse spinel Fe_3O_4 structure.[26,35,36] Table 2 presents the T_{max} values for the reduction peaks and the cumulative uptake of H_2 for these peaks. The theoretical amount of mol H_2 consumed per Fe for this step is 0.167. From our results it is clear that H_2 consumption during the first reduction step of the Fe_2O_3–Cu sample is too high to be accounted to the reduction of Fe_2O_3 to Fe_3O_4 (0.25 instead of 0.167 mol H_2/mol Fe). Since, on the basis of the molar ratios of Fe and Cu, an extra consumption of ~0.05 mol H_2, the difference is explained by the reduction of CuO to Cu_2O and metallic Cu[37] (theoretical uptake 1 mol H_2 per mol of Cu). This step is resolved as a shoulder in reduction pattern.

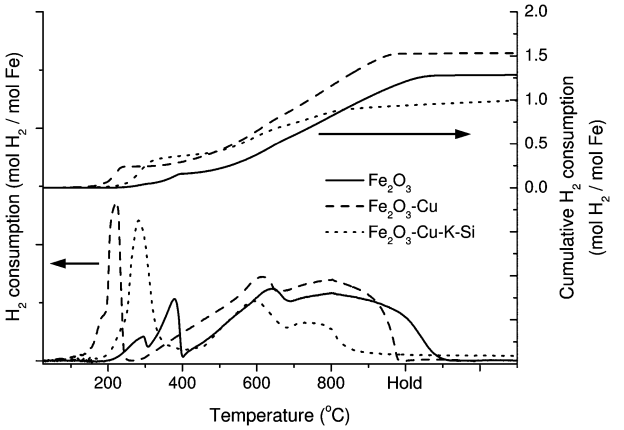

Fig. 1 H_2 temperature programmed reduction profiles and cumulative H_2 consumption curves of the three catalysts under investigation.

The high H_2 consumption in the first reduction step of the Fe_2O_3–Cu–K–Si catalyst is only partially (~0.07 extra consumption is expected from CuO species) explained by the reduction of the CuO that is present in the catalyst. The higher consumption in this case might be due to the partial reduction to FeO species in close contact with the SiO_2 support,[22] with a theoretical uptake of 0.5 mol H_2 per mol of Fe. The second reduction step is shifted to lower temperatures for the Fe_2O_3–Cu catalysts, with a final uptake of 1.53 after the experiment *vs.* 1.3 in the case of the unpromoted catalyst. The theoretical H_2 uptake for the total reduction of Fe_2O_3 to Fe is 1.5. The higher total uptake is explained by the consumption of H_2 in the reduction of CuO. The Fe_2O_3–Cu–K–Si catalyst shows a suppressed amount of H_2 uptake at higher temperatures, indicative for a limited extent of reduction beyond Fe^{2+}. As an indication for the total extent of reduction of the catalysts, Fig. 1 also shows the total cumulative amount of H_2 uptake during the TPR experiment. From this, the influence of Cu on the bulk reduction properties of the materials is clearly resolved. Both reduction steps, from Fe^{3+} to Fe^{2+} and Fe^{2+} to Fe^0, are facilitated in the presence of Cu, with the second reduction step being retarded in the presence of SiO_2.

TEM analysis provided more insight into the morphological changes of the catalysts. Both unsupported samples show large agglomerates (~200–400 nm) of very small (~5 nm, see ESI†, Fig. E1) iron oxide crystallites, as well as some larger crystallites (~50 nm). The Fe_2O_3–Cu–K–Si sample shows similar morphology. However, no large crystallites are observed in this case. EDX analysis confirmed that the Cu and Fe phases

Table 1 Physicochemical properties of the three materials under investigation after calcination and after CO–H_2 treatment

Catalyst sample	Molar composition (at.%)	BET surface area/m^2 g^{-1}	Pore volume[a]/mL g^{-1}
Fe_2O_3	Fe = 100	136	0.17
after CO–H_2		7	0.05
Fe_2O_3–Cu	Fe = 96.3; Cu = 3.7	164	0.19
after CO–H_2		11	0.08
Fe_2O_3–Cu–K–Si	Fe = 77.5; Cu = 5.8; K = 4.6; Si = 12.1	297	0.83
after CO–H_2		39	0.10

[a] As calculated from the N_2 desorption isotherm.

Table 2 Temperature programmed reduction analysis of the catalysts under study

Catalyst sample	Peak T_{max}/°C	H_2 uptake[a] (mol H_2/mol Fe)
Fe_2O_3	290	0.06
	377	0.16
	640	0.68
	800+	1.30
Fe_2O_3–Cu	220	0.25
	613	0.70
	800+	1.53
Fe_2O_3–Cu–K–Si	283	0.39
	591	0.78
	734	1.01

[a] Cumulative uptake of H_2.

in the Fe_2O_3–Cu sample were well mixed, while selected area diffraction analysis confirmed the presence of crystalline α-Fe_2O_3, even in the Fe_2O_3–Cu–K–Si sample. Because of the low contrast between SiO_2 and α-Fe_2O_3 it is not possible to straightforwardly distinguish between the two phases in the TEM images. However, EDX analysis showed that all phases in the Fe_2O_3–Cu–K–Si catalyst were homogeneously distributed.

After treatment in 0.4 mbar CO–H_2 TEM images of the Fe_2O_3 and Fe_2O_3–Cu catalysts showed significant sintering of the Fe phases and the formation of crystallites in the size range of 50–100 nm (see ESI†, Fig. E2).

The Fe_2O_3 sample consisted of large α-Fe crystallites. EDX results showed some contribution of carbon and oxygen species in the catalyst. Some contribution of oxygen is expected on the surface layer of the catalyst, due to the formation of a thin Fe_3O_4 layer when the catalyst material is carefully passivated.[38] In addition, some unreduced larger Fe_3O_4 crystallites were found as well.

TEM-EDX analysis of the Fe_2O_3–Cu catalyst also showed a contribution of carbon and oxygen species. It was observed that Cu clusters were formed in the catalyst material after the treatment. Cu clusters were mainly present where carbon was found, and some specific regions were found which consisted of Fe–Cu clusters surrounded by a type of filamentous carbon. The Fe_2O_3 catalyst did not show the deposition of this type of carbon, suggesting an important role of Cu in this process. The formation of filamentous carbon has been observed to be enhanced in Fe–Cu bimetallic catalysts as compared to catalysts without Cu.[13]

The Fe_2O_3–Cu–K–Si material showed the formation of small ~5 nm, as well as some larger crystallites. Detailed analysis of the TEM images was very difficult due to the small cluster sizes and low contrast between the Fe phases formed after the CO–H_2 treatment and the SiO_2 support. Along with very small Cu clusters homogeneously distributed over the material, some larger Cu agglomerates (~10 nm) were also observed. The secondary electron detector showed that the surface of the catalyst was relatively smooth and, in combination with the observation of carbon and oxygen species, it is likely that the surface of the catalyst is covered with a carbonaceous layer after the treatment.

Fig. 2 shows the XRD patterns of the three catalysts before and after the *in situ* XAS/XPS experiment. In all calcined catalysts, the presence of α-Fe_2O_3 was confirmed. The freshly calcined Fe_2O_3–Cu–K–Si catalyst shows very broad reflections at the 40° and 75° 2θ, suggesting the presence of very small Fe_2O_3 crystallites, in accordance with TEM.

Scherrer analysis yielded crystalline domain sizes of ~70 nm for the Fe_2O_3 catalyst and ~40 nm for the Fe_2O_3–Cu catalyst. The peaks in the diffractogram of the Fe_2O_3–Cu–K–Si catalyst were too broad to reliably estimate crystallite domain sizes, however, it can be expected that the sizes involved are well below 5 nm. Furthermore, it is noted here that especially for the Fe_2O_3–Cu catalyst, except for well crystallized material, there is most likely also a significant amount of smaller/amorphous material, as suggested by the very broad features around 40° and 75° 2θ, underlying the sharper diffraction peaks. This suggests that the addition of Cu has an effect on the particle size and/or crystallinity of the material, in line with the observations from TEM and N_2-physisorption. Furthermore, no crystalline CuO phase is observed, indicating that the Cu is intimately mixed with the

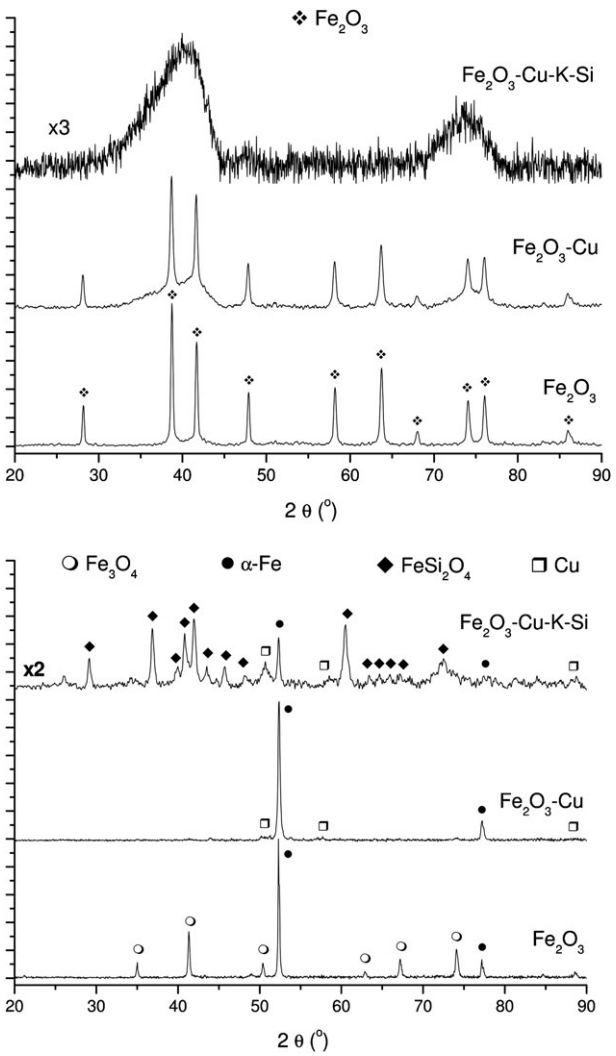

Fig. 2 X-Ray powder diffraction patterns of the three catalysts under investigation after calcination and after their respective treatments in 0.4 mbar CO–H_2.

Fe_2O_3 phase, as can be expected from the co-precipitation preparation method that was used.

After treatment in 0.4 mbar CO–H_2, the Fe_2O_3 sample, apart for an α-Fe phase, characterized by two peaks at 52.4° and 77.3° 2θ, contains a significant contribution of the Fe_3O_4 inverse spinel phase (main peak at 41.4° 2θ). In the Fe_2O_3–Cu catalyst, only the α-Fe crystal phase, along with some metallic (fcc) Cu (peaks at 50.8°, 59.4° and 88.9°) is detected. The estimated α-Fe crystallite sizes after treatment were ~80 nm for the Fe_2O_3–Cu catalyst material and ~100 nm for the Fe_2O_3 catalyst material, in agreement with the TEM results.

Based on the diffraction results and the H_2 TPR results, it is clear that the Cu phase, which was intimately mixed with the iron oxide phase, facilitates the reduction of the catalyst bulk phases to α-Fe. Although there is an influence of Cu on the texture of the catalyst material, as judged from N_2-physisorption and XRD patterns presented here, this influence alone does not account for the dramatic change in redox properties of the materials and therefore the enhanced reduction rate is not only textural in nature.

The Fe_2O_3–Cu–K–Si catalyst, as expected, still shows a much lower crystallinity after the reduction treatment. In this sample there are main contributions of metallic Cu, α-Fe and crystalline Fe_2SiO_4 (fayalite, main peak at 42° 2θ) resolved. The α-Fe crystallite size in this case was about 60 nm, though significantly smaller clusters were also present, as judged from the high diffraction background in combination with the TEM results. A small contribution of the χ-Fe_5C_2 phase[39] to the diffraction pattern could not be excluded. The observation of the formation of crystalline Fe_2SiO_4 is a remarkable one and merits further research, since the phase is usually only reported at high temperatures and reported to be very sensitive to the partial pressure of oxygen.[40]

3.2 *In situ* X-ray absorption spectroscopy

In order to characterize changes in the (near-)surface structure of the catalyst during reduction, X-ray absorption spectroscopy was performed at the Fe $L_{3,2}$, Cu $L_{3,2}$ and O K-edges using conversion electron yield (CEY) detection mode. Before the reduction experiment, the three catalysts consisted of a pure Fe^{3+} hematite phase, as evidenced from the 709.3 eV feature in the Fe L_3-edge and a characteristic double pre-edge feature in the O K-edge spectra (529.4 and 530.7 eV) (see ESI†, Fig. E3), ascribed to the oxygen 2p weight in states of 3d character.[41,42] An enhanced spectral feature in the O K-edge of the Fe_2O_3–Cu–K–Si catalysts at ~537 eV indicated the presence of SiO_2.

In the Cu-containing catalyst samples, the Cu phase was mainly present as Cu(II)O, as evidenced by the L_3-edge peak (Fig. 3d and e) at 931.3 eV[43,44] and a small contribution in the pre-edge region of the O K-edge spectra at 530.1 eV.[41] In addition, a contribution was visible in the Cu L_3-edge at 933.7 eV, indicating a minor presence of Cu(I) species.

Fe $L_{3,2}$-edges. Fig. 3a–c shows the evolution of the Fe $L_{3,2}$-edges of the different catalysts as a function of gas composition and temperature. Up to 180 °C in 0.4 mbar H_2, the spectrum of the Fe_2O_3 material shows very little change. In the Fe_2O_3–Cu catalyst material, however, some change is observed in the absorption feature at 707.9 eV, characteristic for Fe^{2+} species and pointing to the conversion of the α-Fe_2O_3 to Fe_3O_4.[22,45,46] Upon switching to 0.4 mbar CO–H_2, both Fe_2O_3 and Fe_2O_3–Cu samples undergo progressive reduction to Fe^0 (with a characteristic absorption in the L_3-edge at 706.8 eV[22,45,46]). Overall, the reduction of the Cu-promoted catalyst is significantly more facile with the reduction being complete after treatment at 275 °C for 0.5 h. The final reduction step in the unpromoted catalyst sample was slower and only complete after 1 h at 275 °C.

The Fe L-edge spectrum of the Fe_2O_3–Cu catalyst after treatment in CO–H_2 at 275 °C for 1 h showed a small contribution of Fe_3O_4, visible as a shoulder at ~709 eV (see ESI†, Fig. E4), while the Fe_2O_3 catalyst did not show any contribution of this phase. This suggests that the Cu-containing catalyst, although its bulk reduces more quickly than the unpromoted catalyst, might be slightly oxidized on the surface after reduction in the CO–H_2 mixture. An explanation for this higher susceptibility to oxidation of the reduced Fe phase in the presence of Cu will be discussed in conjunction with the *in situ* XPS results.

The Fe_2O_3–Cu–K–Si catalyst shows quite distinct reduction behavior from the other two materials. At ~180 °C a significant amount of the catalyst is reduced to Fe_3O_4. However, after 1 h in 0.4 mbar CO–H_2 at 275 °C, the reduction of the catalyst material has not significantly progressed further than the Fe_3O_4 phase. A relatively low CO_2/H_2O ratio was observed from MS (ESI†, Fig. E5) during the treatment at 275 °C, suggesting a more important role of H_2 in the reduction process. However, since XAS shows that only a small amount of the Fe_3O_4 phase reduces at that point and, at the same time, progressive reduction to Cu_2O and Cu^0 is observed, the low CO_2/H_2O ratio is likely to be solely due to the reduction of Cu_2O and suggests that this phase is preferentially reduced by H_2 under our conditions. Further increasing the reduction temperature to 350 °C resulted in increasing absorption features in the XAS spectra, characteristic for Fe^{2+} and Fe^0. The majority of the spectrum, however, remained unchanged. Linear combination fitting yielded an average final composition of ~75% Fe_3O_4, 20% Fe^{2+} and 5% Fe^0 after 1 h reduction at 350 °C.

Similar to what was observed in the TPR experiment and XRD, the presence of small Fe_2O_3 particles in close contact with the SiO_2 phase significantly retards the reduction of this phase to Fe^0 and stabilizes Fe^{2+} species through the formation of mixed Fe(II)silicate species.[22,47]

Cu L_3-edge. As the Cu L_2-edge showed analogous changes compared to the L_3-edge, from this point on we will discuss only the Cu L_3-edge structure. The evolution of the Cu L_3-edge during reduction treatment of the Cu-promoted catalysts are shown in Fig. 3d and e. In the Fe_2O_3–Cu catalyst, the spectral feature at 931.3 eV, characteristic for CuO, decreases during the initial H_2 treatment at the expense of a broad peak at 933.7 eV, characteristic for Cu^+ in Cu_2O.[43,44] At 180 °C in CO–H_2, however, there is still a significant contribution of CuO to the spectrum. From 200 °C, a third contribution to the spectrum is observed. This contribution with the edge position at 932.7 eV is characteristic for metallic Cu.[43] At 275 °C, a

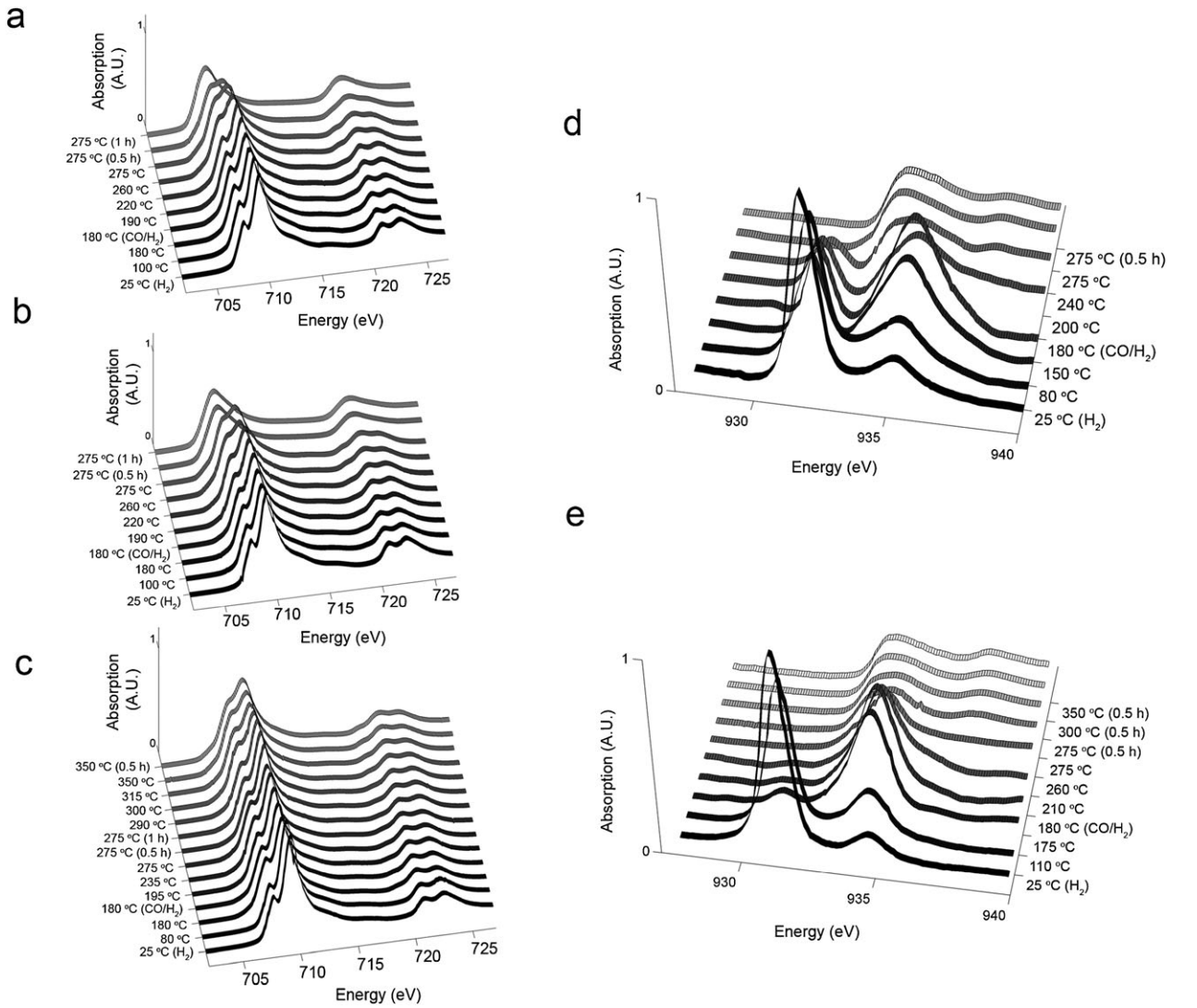

Fig. 3 Fe $L_{3,2}$-edge (a–c) and Cu L_3-edge (d and e) X-ray absorption spectra of the different catalysts under investigation during treatment in 0.4 mbar CO–H_2. (a) Fe_2O_3, (b and d) Fe_2O_3–Cu, (c and e) Fe_2O_3–Cu–K–Si.

significant amount of the sample has been converted to metallic Cu with some residual CuO being present. After 0.5 h at 275 °C, all CuO has been converted to metallic Cu.

The Cu species in the Fe_2O_3–Cu–K–Si catalyst sample show a quite different reduction behavior from the Fe_2O_3–Cu catalyst sample. At 180 °C, all CuO species have been converted to Cu_2O species and there is only a small contribution of Cu^0 species. The second reduction step to Cu^0 seems to be significantly delayed (only significant at 260 °C) compared to the Fe_2O_3–Cu catalyst sample which started forming Cu^0 from 200 °C. Although the reduction of CuO to Cu_2O is significantly faster in the Fe_2O_3–Cu–K–Si catalyst, indicative for smaller CuO particles, Cu_2O species are stabilized by strong interactions with the SiO_2 phase and this delays the reduction step to Cu^0. This has important implications for the reduction properties of this catalyst, as will be further discussed in combination with the *in situ* XPS results.

It can be seen in Fig. 3 that the reduction to Cu^0 marked the onset of the reduction of the iron oxide phase in both Cu-promoted samples. In the Fe_2O_3–Cu catalyst, the reduction to Cu^0 parallels a significant increase in the contribution of Fe^0 to the spectrum. This increase is rationalized by the formation of metallic Cu nuclei[10,15,27] which can adsorb H_2 (dissociatively) and CO (associatively). Because of this, adsorbed H_2 and CO species can 'spillover' to phases in the proximity of the Cu sites and thereby facilitate reduction of the Fe phase. The latter point will be discussed further under the O(1s) and C(1s) XPS results.

The observed facilitation of the first reduction step, from α-Fe_2O_3 to Fe_3O_4, is not readily explained by the formation of metallic nuclei, as in our *in situ* experiment this step takes place before the CuO species are reduced to Cu^0 ($\sim$200 °C in the Fe_2O_3–Cu catalyst). Therefore, the difference in reduction behavior between the two samples is likely to be due to differences in starting α-Fe_2O_3 crystallinity and/or the involved particle sizes rather than to the aforementioned effects of Cu. The smaller, less crystalline α-Fe_2O_3 particles in the Cu-promoted samples are reduced to Fe_3O_4 in a more

facile manner, as is also observed in the case of the poorly crystalline SiO_2-containing Fe_2O_3–Cu–K–Si catalyst material.

O K-edge. The O K-edge spectra of the Fe_2O_3 and Fe_2O_3–Cu catalysts after reduction treatment show only a minor contribution of the pre-edge peak (see ESI†, Fig. E6) indicating that most oxide phases have been reduced. This can be expected from the Fe L-edge results, which indicated (almost) complete reduction of the iron oxide phase in the two samples. The characteristic O K-edge spectrum shape of the Fe_2O_3–Cu–K–Si catalyst after reduction at 350 °C confirms that the oxidic species are mainly present as a mixture of pure octahedral Fe^{2+} [48] and Fe_3O_4[41] species. A small contribution of SiO_2 (~537 eV) is also resolved in the spectrum.

3.3 *In situ* X-ray photoelectron spectroscopy

The XPS results will be discussed in two parts. We will first focus on the characterization of the catalyst phases and the role of Cu on the surface structure of the catalysts during reduction in CO–H_2. After this, we will consider the surface properties of the catalysts with respect to the carbon and oxygen surface species.

3.3.1 Catalyst phases as studied by Fe(2p), Cu(2p), Si(2p) and K(2p) XPS

Fe(2p) XPS. Fig. 4 shows the Fe $2p_{3/2}$ and $2p_{1/2}$ spectral lines of the three catalysts during the reduction run. The spectra were acquired using 1200 eV incident photon energy, corresponding to an IMFP of 10 Å. Upon reaching 275 °C, the three samples show a contribution of Fe^{2+} and Fe^{3+} species as evidenced from the contributions at 709.0 and 711.0 eV to the Fe $2p_{3/2}$ peak. The contribution of Fe^{3+} species to the XPS spectrum at this point decreases in the order Fe_2O_3–Cu–K–Si > Fe_2O_3–Cu > Fe_2O_3. The surface of both Si-free catalysts is reduced to metallic Fe after 1 h at 275 °C, as observed from the main $2p_{3/2}$ contribution at 706.8 eV.

Even after treatment in 0.4 mbar CO–H_2 at 350 °C, the surface of the Fe_2O_3–Cu–K–Si catalyst consists of mainly Fe^{2+}, with some Fe^{3+} being present. XRD after treatment at 350 °C, however, does not show crystalline Fe^{3+} bearing Fe_3O_4 or α-Fe_2O_3 phases, suggesting that the Fe^{3+} species are present in very small or amorphous Fe_3O_4 particles. Strong interactions between the SiO_2 and iron oxide phase inhibit the reduction of iron oxide species beyond Fe^{2+}, as also suggested by the other techniques. XRD analysis does show a presence of Fe_2SiO_4 and minor amounts of α-Fe. Therefore, since no significant contribution of Fe^0 was observed in XPS (probing ~10 Å deep) and only a small contribution was observed in XAS (probing 40 Å deep) the surface of the metallic particles might be covered by a Fe_2SiO_4 overlayer.[22,47]

As was observed in the XAS data, the surface of the Fe_2O_3–Cu sample has a contribution of $Fe^{2+/3+}$ species after reduction. After evacuation, the surface is even briefly oxidized, as evidenced by the strong shoulder in the spectrum at 710.6 eV. The Fe_2O_3 and (not completely reduced) Fe_2O_3–Cu–K–Si catalyst samples do not show surface reoxidation during evacuation.

The surface nature of the oxidation layer of the Fe_2O_3–Cu catalyst is even more evident when the surface is probed with a lower incident energy: 850 eV, corresponding to an IMFP of 5 Å. Fig. 4d shows the Fe $2p_{3/2}$ and $2p_{1/2}$ XPS region probed at 850 eV incident energy for the three catalyst samples after evacuation after their respective reduction treatments. The oxidation of the Fe surface species was shown to be reversible (Fig. 4b). It was observed that after exposure to vacuum for prolonged times, the thin surface oxide layer was removed and the sample reduced back to metallic Fe. Possibly, the removal of surface adsorbates and/or hydroxyl groups (further characterized below) at high temperature and vacuum is sufficient to reduce the sample back to its metallic state.

Cu(2p) XPS. As expected from the XAS data, the Cu $2p_{3/2}$ and $2p_{1/2}$ XPS spectra of the Cu-promoted catalysts (see ESI†, Fig. E7) showed the characteristic Cu^0 peaks at 932.7 and 952.3 eV after treatment in CO–H_2 at 275 °C. No remaining CuO or Cu_2O was observed.

While the surface Fe phase of the Fe_2O_3–Cu catalyst was oxidized upon evacuation, no signs of oxidation of the Cu^0 were observed from XPS. It was also observed that the surface distribution of the Cu phase was quite distinct for the supported and unsupported catalysts.

Table 3 summarizes the Cu/Fe ratios for the two catalysts at different stages of the reaction. The atomic ratios were compared at an IMFP of ~5 Å. The decrease in Cu/Fe ratios in the Fe_2O_3–Cu–K–Si catalyst at higher temperatures can be ascribed to agglomeration of the Cu phase and/or spreading to the support material at higher temperatures.[10] In the unsupported catalyst, the Cu phase segregates to the surface, as is predicted[49] for the two non-alloying[50] metals. Though this is opposite to the observations by Wielers *et al.*,[12,13] the discrepancy between the two results is likely found in the lower pressures applied here and the presence of both CO and H_2.

Si(2p) XPS. The Si $2p_{3/2}$ peak at ~103.3 eV[51,52] was used to calculate the atomic ratios of Fe/Si and Cu/Si in the Fe_2O_3–Cu–K–Si catalyst. The ratios, referring to the atomic ratios at an IMFP of ~10 Å, are reported in Table 4.

The Fe/Si as well as the Cu/Si ratios increase upon increasing reduction times and higher temperature treatment. Both suggest surface enrichment of Cu and Fe species on the SiO_2 support. In combination with the decreasing Fe/Cu ratios, this indicates segregation of the Cu and Fe phases on the SiO_2 support, as also observed in TEM. The Cu phase on the SiO_2 cannot "spillover" dissociated H_2 and CO to the Fe_3O_4 particles in the catalyst efficiently. Therefore, the combination of the strong interaction between SiO_2 and the Fe phase, as evidenced from the observation of Fe^{2+} species in XAS and XPS and the formation of Fe_2SiO_4 in XRD, and the segregation of Cu to the SiO_2 phase, is responsible for the slow reduction of iron oxide phases in this catalyst material.

K(2p) XPS. The Fe_2O_3–Cu–K–Si catalyst shows a doublet at 293.9 and 296.6 eV, assigned to metastable basic potassium carbonate species.[53,54] The peaks shift to slightly higher binding energies (294.2 and 297.0 eV, respectively) upon treatment at 350 °C (Fig. 5).

These binding energy values, however, are too low to be assigned to elemental K and, moreover, no plasmon lines characteristic for elemental K are observed. Therefore, in

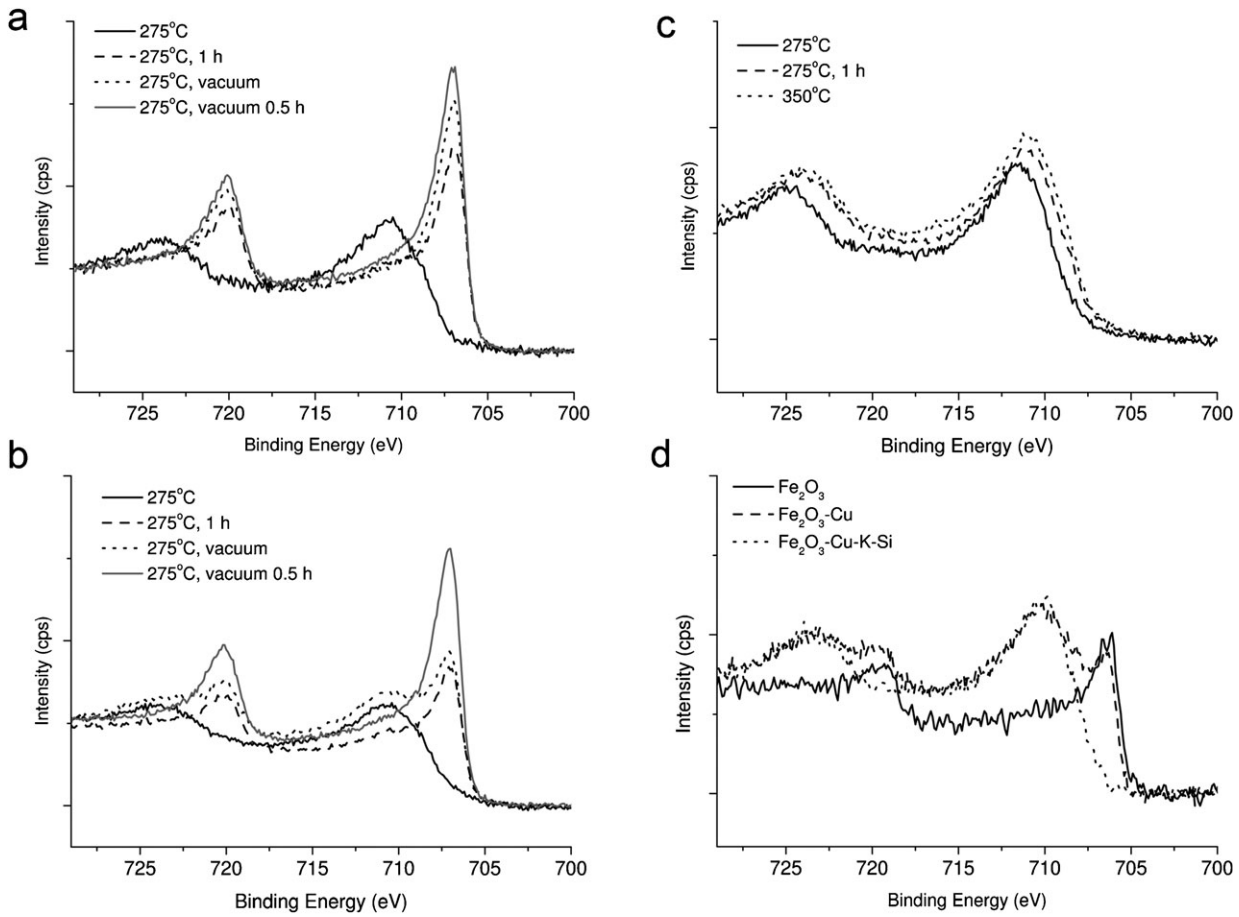

Fig. 4 Fe(2p) XPS spectra of the three materials under investigation during reduction in 0.4 mbar $CO–H_2$ using an incident X-ray energy of 1200 eV: (a) Fe_2O_3, (b) Fe_2O_3–Cu, (c) Fe_2O_3–Cu–K–Si and (d) the three catalyst immediately after evacuation, examined with an incident X-ray energy of 850 eV.

Table 3 XPS Cu/Fe atomic ratios of the Cu-promoted catalysts

Catalyst sample	Fe_2O_3–Cu	Fe_2O_3–Cu–K–Si
275 °C t = 0 h	0.11	0.66
275 °C t = 0.5 h	0.22	—
275 °C t = 1 h	0.46	0.50
350 °C	—	0.21

Table 4 XPS Fe/Si and Cu/Si atomic ratios of the Fe_2O_3–Cu–K–Si catalyst material after different steps in the reduction treatment

Catalyst sample	Fe/Si (~10 Å)	Cu/Si (~10 Å)
275 °C t = 0 h	0.35	0.27
275 °C t = 1 h	0.45	0.37
350 °C	1.77	0.54

combination with the observations in the O(1s) region discussed below, we conclude that at higher temperatures, K is present as KOH, and/or strongly interacting with the SiO_2 support. Although bulk K_2CO_3 does not decompose to KOH below 500 °C, the role of KOH as an active promoter phase in Fe-based catalysts has been suggested in the literature.[53–55] The K : Fe ratios decrease dramatically, from ~1 to ~0.3 upon treatment at 350 °C, suggesting decomposition of the K_2CO_3 phase and spreading of the K species over the catalyst.[54]

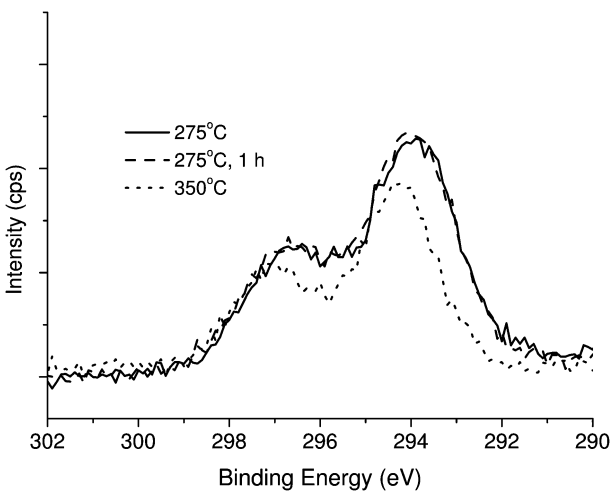

Fig. 5 K(2p) XPS spectra of the Fe_2O_3–Cu–Si–K catalyst during the different stages of $CO–H_2$ treatment.

3.3.2 Surface reactant species as studied by O(1s) and C(1s) XPS

O(1s) XPS. The O(1s) region of the catalysts showed two main peak contributions (see ESI†, Fig. E8): one at 530.2 eV and a shoulder at 531.7 eV. The peak at 530.2 eV is

characteristic for oxidic species while the 531.7 eV peak is ascribed to the presence of adsorbed H_2O species on the surface of the catalyst or surface hydroxyl groups.[56–58] The SiO_2-containing catalyst showed a more pronounced feature at 531.8 eV, a slightly higher energy than the other catalysts. This is ascribed to the presence of surface silanol groups. The surface nature of these features was examined by probing the surface at different incident X-ray energies, and thus different kinetic energies of the created photoelectrons. The relative contribution of the 531.7 eV peak compared to the 530.2 eV peak in all samples was higher at 7 Å (850 eV incident energy) compared to 10 Å (1200 eV incident energy), confirming the surface nature of these species. The O/Fe and OH/Fe ratios for the catalysts after reduction are summarized in Table 5. The SiO_2-containing catalyst showed lower OH and O ratios after treatment at 350 °C. This is indicative of a high amount of residual oxidic species (Fe_3O_4/Fe_2SiO_4) after the reduction treatment in combination with the dehydroxylation of silanol groups and other hydroxyl species under high temperature/low pressure conditions.[47] In all catalysts, the O/Fe ratios decreased after reduction. However, especially in the case of the Cu-promoted catalysts, the contribution of oxygen was still significant after treatment at 275 °C for 1 h. Both Cu-containing catalysts also showed that the O(1s) contribution initially increased upon reduction, and this might indicate the physisorption of H_2O, other oxygen bearing species, or the presence of surface OH groups during the reduction treatment. The increase in the O(1s) contribution might also reflect the enhanced associative adsorption of CO in the presence of Cu^0, supporting a CO spillover mechanism. In further support of this, it is interesting to note that the Fe(2p) and Cu(2p) XPS spectral regions and the O K-edge XAS shape only a small extent of oxidation during CO–H_2 exposure, something that one might expect in the case of the observed high atomic O/Fe ratios. This suggests that under our 0.4 mbar CO–H_2 conditions, the surface of the catalyst is very dynamic and surface oxygen species are very quickly adsorbed and desorbed. Our MS data (see ESI†, Fig. E5) supports this, as CO_2 and H_2O evolution rates were higher for the Fe_2O_3–Cu catalyst compared to the Fe_2O_3 catalyst.

C(1s) XPS. The C(1s) region showed significant differences for the three catalysts during treatment in CO–H_2. The relevant XPS regions and the evolution of total C/Fe ratios (both probed at an IMFP of 10 Å; 1200 eV for Fe(2p), 850 eV for C(1s)) of the three catalysts during treatment for 1 h at 275 °C are shown in Fig. 6. The signal intensities of the C(1s) XPS shapes are normalized to the Fe(2p) peak area for each catalyst.

Except for the presence of the characteristic Cu $L_3M_{45}M_{45}$ Auger peak (kinetic energy 918 eV, 282 eV "binding energy"),

Table 5 XPS O/Fe and OH/Fe atomic ratios of the three catalysts under investigation after the CO–H_2 treatment

Catalyst sample	Fe_2O_3	Fe_2O_3–Cu	Fe_2O_3–Cu–K–Si
O/Fe ratio (~10 Å)	0.31	0.66	4.57 (275 °C) 2.67 (350 °C)
OH/Fe ratio (~10 Å)	0.37	0.72	5.54 (275 °C) 2.50 (350 °C)

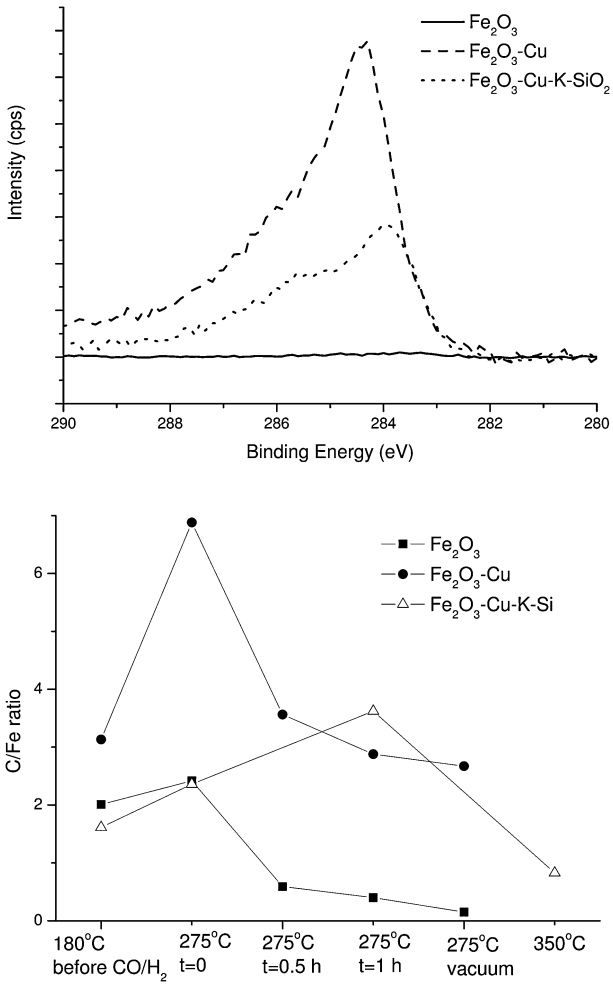

Fig. 6 Top: C(1s) XPS spectra (incident energy 850 eV) of the catalysts after treatment in 0.4 mbar CO–H_2 at 275 °C for 1 h. The counts are normalized to the intensity of the Fe $2p_{3/2}$ peak areas. Bottom: the evolution of C/Fe ratios during treatment.

there were no significant differences between the presented data and the C(1s) data collected at 1200 eV incident energy, constituting an escape depth of ~15 Å, suggesting the absence of chemically different subsurface carbon (or carbide) species under the conditions applied here. In the Fe_2O_3 sample, the carbon species begin to disappear upon reaching 275 °C and are almost completely gone after 2 h at this temperature, followed by evacuation. The Fe_2O_3–Cu and Fe_2O_3–Cu–K–Si catalysts showed a significant amount of residual carbon after the same treatment. Upon going to higher temperatures in the case of the latter catalyst, some carbon is removed from the catalyst surface, as evidenced from the lower C/Fe ratios. However, both Cu-promoted catalysts have C/Fe ratios of ~3 after the reduction treatment at 275 °C.

The data showed the formation of at least three different carbonaceous phases on the surface of the Fe_2O_3–Cu and Fe_2O_3–Cu–K–Si catalysts after heating in CO–H_2 up to 275 °C. The phase characterized by a contribution at 284.7 eV is commonly assigned to graphitic type carbon.[59–62] A contribution of carbon species with a characteristic peak at 283.9 eV was observed in the Fe_2O_3–Cu–K–Si catalyst,

indicating the presence of surface CH_x species.[59] The relatively high amount of these species compared to the other two catalysts might be a result of the smaller particle sizes involved in this material, in combination with the presence of K species. The addition of K has been known to increase the heat of chemisorption of CO on Fe surfaces,[63] increasing carbon deposition rates[54] and increasing the amount of carbon-based surface intermediates.[64]

A third contribution to the C(1s) spectrum, at around 286 eV, has been assigned to carbon directly coordinated to oxygen,[65] and might suggest the presence of oxo-radical or carbonate-like species, as discussed by Bonzel and Krebs[59] or associatively bonded CO. In view of this, the high O/Fe and OH/Fe ratios observed in the Cu-promoted catalysts might be due to the presence of these surface species. As in this case oxygen is coordinated directly to carbon species instead of the Fe or Cu metal sites this would explain the observation of mainly reduced Fe and Cu species in XPS despite the high O/Fe and OH/Fe ratios. There is some more supporting evidence for the formation of these species under our reaction conditions. First, the intermediate heat of adsorption of CO[21,66] on Cu, in combination with the high surface concentration of Cu species, might enhance the water-gas shift activity during $CO–H_2$ flow and therefore the Fe surface might be (partially) covered with surface hydroxyl groups and (associatively bonded) CO. MS results (see ESI†, Fig. E5) show that the CO_2/H_2O ratio was relatively high in the case of the Cu-promoted catalyst. This is a strong indication for enhanced WGS reactivity in the Cu-promoted catalysts. Upon evacuation, in the absence of reactive gas phase CO and H_2 molecules, the Fe surface might oxidize temporarily. This oxidation reaction is reversible, however; as upon prolonged exposure to vacuum the surface of the catalyst reduces back to its metallic state, possibly due to the dehydroxylation of the Fe surface. This suggests a weak interaction between the oxygen species observed in XPS and the Fe surface.

In the catalyst without Cu, the lower concentration of oxygen surface species and the higher amount of dissociatively adsorbed CO might lead to a higher methanation rate and a lower susceptibility to oxidation upon evacuation. The concentration of CH_4 in the exit flow from the reaction chamber, as measured by MS, was indeed higher and stable for 2 h in the case of this catalyst while the CO_2 concentration was limited.

In the case of the SiO_2-containing catalyst, the discussion of the role of Cu in the formation of surface C and O bearing species becomes more complicated because of the presence of surface silanol groups, which also contribute to the O(1s) spectrum. In addition, the presence of K influences the adsorption of CO and CO_2 on Fe surfaces[18,63] and therefore might also play an active role in changing surface C and O concentrations.

3.4 Influence of Cu on the surface and bulk structure of the catalysts

Table 6 summarizes the species and phases in the catalysts before and after their respective reduction treatments, as observed from XPS, XAS and XRD. Scheme 1 sketches the surface and near-surface composition on the basis of these observations. From the XRD results it is clear that the addition of Cu decreases the overall bulk crystallinity of the α-Fe_2O_3 phase after calcination and, as a result, Cu acts as a textural promoter and facilitates the reduction of α-Fe_2O_3 to Fe_3O_4. The addition of SiO_2 in combination with Cu has a similar effect, with the initial reduction of very small, amorphous α-Fe_2O_3 particles to Fe_3O_4 proceeding faster than for the unpromoted catalyst. Our results further suggest that metallic Cu particles are responsible for enhancing the rate of the reduction step of bulk Fe_3O_4 to Fe^{2+} and Fe^0, most likely due to a combination of textural and electronic effects.

In the materials before the reduction treatment, Cu is present as CuO species in intimate contact with the Fe_2O_3 phase. The CuO phase is reduced to Cu_2O and Cu^0 under mild conditions in the unsupported catalyst. The formation of the Cu^0 phase marks the onset of the reduction of the Fe_3O_4 phase to Fe^0, most likely through the spillover of H_2 or CO species adsorbed on Cu^0 and/or through a textural promotion mechanism. In the case of the SiO_2 bearing material, Cu_2O species are stabilized with respect to Cu^0 by interaction with the SiO_2 phase and as a result, the reduction of the Fe_3O_4 phase to Fe^0 was delayed. In combination with the observed strong interactions between Fe^{2+} species and SiO_2, resulting in the formation of Fe(II)silicate species, this leads to a poorly reduced catalyst even after treatment in 0.4 mbar $CO–H_2$ at 350 °C.

As mentioned before, the reduction of Fe_2O_3 to metallic Fe was not feasible in either 1 mbar CO or 1 mbar H_2 and a mixture of both gases was used in this study. It is therefore not clear if in our experiments the reduction of the iron oxide phase by H_2 or by CO is dominant. We will consider both cases below.

MS (see ESI†, Fig. E5) showed high CO_2/H_2O ratios during reduction of the unsupported Cu-containing Fe_2O_3–Cu catalyst and the relatively high C/Fe and O/Fe XPS ratios suggest that the reduction reaction by CO is dominant in the presence of Cu. However, an alternative explanation for this observation is the enhancement of the WGS reaction in the presence of Cu^0, due to the higher amount of associatively bonded CO species present. Both cases, however, point to a CO spillover by Cu. It is noted here, however, that it cannot be excluded that some CO_2 evolution might also be due to the laydown of carbonaceous deposits (as observed, to some extent, in TEM) on the reduced Fe phase by the Boudouard reaction ($2CO \rightarrow CO_2 + C$).

Therefore the other possibility for the enhanced reduction of iron oxide in the presence of Cu^0 is H spillover from Cu^0 sites. Judging from the higher adsorption energy of H compared to CO on metallic Cu,[21] and the preferential reduction of the CuO phase by H_2 in our experiment, one might expect H_2 spillover from Cu sites to play a larger role in promotion of the reduction process than CO spillover. However, we cannot unambiguously conclude which effect is dominant from our results.

The surface of the Cu-containing unsupported iron oxide catalyst is slightly oxidized after reduction in $CO–H_2$, in contrast to the unpromoted catalyst, which is fully reduced to Fe^0 on the surface. Strikingly, the *bulk* of the Cu-promoted

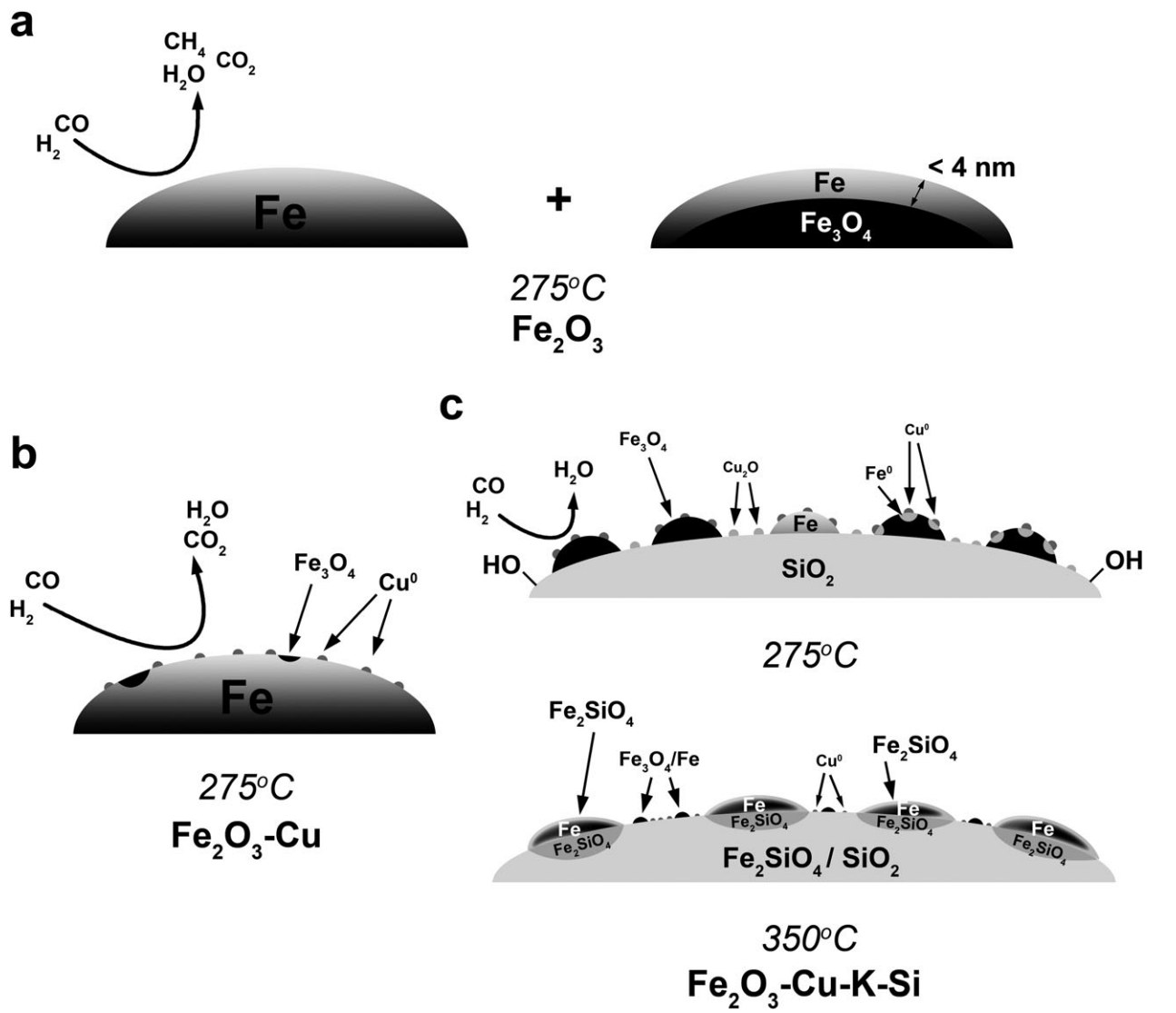

Scheme 1 Schematic overview of the surface and bulk structure of the three different catalysts under study after treatment in 0.4 mbar CO–H_2 for 1 h at the indicated temperatures: (a) Fe_2O_3, (b) Fe_2O_3–Cu and (c) Fe_2O_3–Cu–K–Si.

catalyst is fully reduced to α-Fe, while the unpromoted catalyst contained a significant amount of Fe_3O_4. The reduced Cu species spread to the surface of the metallic Fe phase in the Fe_2O_3–Cu catalyst. This is also the case for the supported catalyst when treated at 275 °C. However, when treated at 350 °C, the Cu phase agglomerates and segregates from the Fe (Fe^{2+} and Fe_3O_4) phases, covering part of the SiO_2 material after treatment. In addition the formation of Fe_2SiO_4 prevents

Table 6 Overview of the surface species and bulk phases as deduced from XPS, XAS and XRD experiments on the three different catalysts under investigation before and after reduction in 0.4 mbar CO–H_2 at 275 and 350 °C

Catalyst material	Technique	Surface species and bulk phases observed		
		Before reduction	0.4 mbar CO–H_2, 275 °C, 1 h	0.4 mbar CO–H_2, 350 °C, 1 h
Fe_2O_3	XPS	Fe^{3+} (Fe_2O_3)	Fe^0	N/A
	XAS	Fe^{3+} (Fe_2O_3)	Fe^0	N/A
	XRD	α-Fe_2O_3 (~70 nm)	α-Fe (~100 nm), Fe_3O_4	N/A
Fe_2O_3–Cu	XPS	Fe^{3+} (Fe_2O_3), Cu^{2+} (CuO)	Fe^0 (α-Fe), Fe^{2+}, Fe^{3+}(Fe_3O_4), Cu^0	N/A
	XAS	Fe^{3+} (Fe_2O_3), Cu^{2+} (CuO)	Fe^0 (α-Fe), Fe^{2+}, Fe^{3+} (Fe_3O_4), Cu^0	N/A
	XRD	α-Fe_2O_3 (~40 nm)	α-Fe (~80 nm), Cu	N/A
Fe_2O_3–Cu–K–Si	XPS	Fe^{3+} (Fe_2O_3), Cu^{2+} (CuO), K^+ (K_2CO_3), Si^{4+} (SiO_2)	Fe^{2+}, Fe^{3+} (Fe_3O_4), Cu^0, K^+ (K_2CO_3), Si^{4+} (SiO_2)	Fe^{2+}, Fe^{3+} (Fe_3O_4, Fe_2SiO_4), Cu^0, K^+ (KOH), Si^{4+} (SiO_2, Fe_2SiO_4)
	XAS	Fe^{3+} (Fe_2O_3), Cu^{2+} (CuO)	Fe^{2+}, Fe^{3+} (Fe_3O_4), Cu^0, Cu^+ (Cu_2O)	Fe^0 (α-Fe), Fe^{2+}, Fe^{3+} (Fe_3O_4, Fe_2SiO_4), Cu^0
	XRD	α-Fe_2O_3 (<5 nm)	N/A	α-Fe (~60 nm), Cu (~10 nm), Fe_2SiO_4

further reduction. Therefore, at 350 °C, the Cu phase has less interaction with the iron phase and has less influence on the redox and surface properties of the catalyst.

After reduction of the Cu promoted unsupported catalyst, the Cu^0 strongly influences the surface coverage of oxygen and carbon species under our 0.4 mbar $CO–H_2$ conditions. After reduction at 275 °C for 1 h, the unpromoted catalyst produced CH_4 and H_2O while the promoted catalyst mainly produced CO_2 and showed relatively high CO_2/H_2O ratios. This suggests that the Cu except for promoting the reduction of iron oxides also plays an important role in altering the surface chemistry of the reduced catalyst.

4. Conclusions

A combination of *in situ* X-ray photoelectron and X-ray absorption spectroscopy provided a detailed view into the influence of Cu as promoter on the redox and surface properties of Fe-based FTS catalysts. By probing the materials at the surface (XPS and XAS) and bulk (TPR and XRD) scale it was illustrated that Cu promotes the reduction of Fe_2O_3 by a combination of textural and $CO–H_2$ spillover effects, with the former being important in the reduction of Fe_2O_3 to Fe_3O_4 and the latter mainly promoting the reduction of Fe_3O_4 to Fe^0. Cu species behaved quite distinctly in the case of supported and unsupported catalysts. CuO was reduced to Cu^0 at temperatures as low as 200 °C in the unsupported catalyst, while in the supported catalyst this reduction was delayed by the stabilization of Cu_2O species by interaction with the SiO_2 support. This, and the strong interaction between Fe^{2+} and SiO_2, inhibited the reduction of the catalyst beyond Fe_3O_4 and Fe^{2+} (Fe_2SiO_4). Treatment at 350 °C resulted in limited interaction between Cu and Fe species in the supported catalyst, through the agglomeration of Cu^0 and spreading over the support material in combination with the formation of Fe_2SiO_4 overlayers. After reduction, the presence of Cu^0 increased the surface concentration of oxygen and carbon species on the unsupported catalyst, illustrating a more complex role of Cu than only promoting the reduction of Fe.

Acknowledgements

The authors thank the staff of BESSY for their help in carrying out the experiments as well as H. Meeldijk and C. van der Spek for their help in acquiring TEM data. Financial support is acknowledged from the Dutch National Science Foundation (CW-NWO/VICI program) (F.M.F.d.G. and B.M.W.) and Shell Global Solutions (B.M.W.).

Notes and references

1 R. B. Anderson, *The Fischer–Tropsch Synthesis*, Academic Press, New York, 1984.
2 G. P. van der Laan and A. A. C. M. Beenackers, *Catal. Rev. Sci. Eng.*, 1999, **41**, 255–318.
3 E. de Smit and B. M. Weckhuysen, *Chem. Soc. Rev.*, 2008, **37**, 2758–2781.
4 V. U. S. Rao, G. J. Stiegel, G. J. Cinquegrane and R. D. Srivastava, *Fuel Process. Technol.*, 1992, **30**, 83–107.
5 E. van Steen and M. Claeys, *Chem. Eng. Technol.*, 2008, **31**, 655–666.
6 J. W. Niemantsverdriet and A. M. van der Kraan, *J. Catal.*, 1981, **72**, 385–388.
7 H. H. Storch, N. Golumbic and R. B. Anderson, *The Fischer-Tropsch and Related Syntheses*, John Wiley & Sons, Inc., New York, 1951.
8 H. Kölbel and M. Ralek, *Catal. Rev. Sci. Eng.*, 1980, **21**, 225–274.
9 M. E. Dry, in *Catalysis—Science and Technology*, ed. J. R. Anderson and M. Boudart, Springer-Verlag, New York, 1981, vol. 1, p. 159.
10 I. E. Wachs, D. J. Dwyer and E. Iglesia, *Appl. Catal.*, 1984, **12**, 201–217.
11 D. B. Bukur, D. Mukesh and S. A. Patel, *Ind. Eng. Chem. Res.*, 1990, **29**, 194–204.
12 A. F. H. Wielers, C. E. C. A. Hop, J. van Beijnum, A. M. van der Kraan and J. W. Geus, *J. Catal.*, 1990, **121**, 364–374.
13 A. F. H. Wielers, G. W. Koebrugge and J. W. Geus, *J. Catal.*, 1990, **121**, 375–385.
14 S. L. Soled, E. Iglesia, S. Miseo, B. A. DeRites and R. A. Fiato, *Top. Catal.*, 1995, **2**, 193–205.
15 S. Li, A. Li, S. Krishnamoorthy and E. Iglesia, *Catal. Lett.*, 2001, **77**, 197–205.
16 R. J. O'Brien and B. H. Davis, *Catal. Lett.*, 2004, **94**, 1–6.
17 H. Hayakawa, H. Tanaka and K. Fujimoto, *Appl. Catal., A*, 2006, **310**, 24–30.
18 C. H. Zhang, Y. Yang, B. T. Teng, T. Z. Li, H. Y. Zheng, H. W. Xiang and Y. W. Li, *J. Catal.*, 2006, **237**, 405–415.
19 K. Pansanga, N. Lohitharn, A. C. Y. Chien, E. Lotero, J. Panpranot, P. Praserthdam and J. G. Goodwin, *Appl. Catal., A*, 2007, **332**, 130–137.
20 E. de Smit, A. M. Beale, S. Nikitenko and B. M. Weckhuysen, *J. Catal.*, 2009, **262**, 244–256.
21 D. Tománek, S. Mukherjee, V. Kumar and K. H. Bennemann, *Surf. Sci.*, 1982, **114**, 11–22.
22 E. de Smit, I. Swart, J. F. Creemer, C. Karunakaran, D. Bertwistle, H. W. Zandbergen, F. M. F. de Groot and B. M. Weckhuysen, *Angew. Chem., Int. Ed.*, 2009, **48**, 3632–3636.
23 E. de Smit, I. Swart, J. F. Creemer, G. H. Hoveling, M. K. Gilles, T. Tyliszczak, P. J. Kooyman, H. W. Zandbergen, C. Morin, B. M. Weckhuysen and F. M. F. de Groot, *Nature*, 2008, **456**, 222–225.
24 H. Bluhm, M. Hävecker, A. Knop-Gericke, M. Kiskinova, R. Schlögl and M. Salmeron, *MRS Bull.*, 2007, **32**, 1022–1030.
25 A. Knop-Gericke, M. Hävecker, T. Schedel-Niedrig and R. Schlögl, *Catal. Lett.*, 2000, **66**, 215–220.
26 O. J. Wimmers, P. Arnoldy and J. A. Moulijn, *J. Phys. Chem.*, 1986, **90**, 1331–1337.
27 N. W. Hurst, S. J. Gentry, A. Jones and B. D. McNicol, *Catal. Rev. Sci. Eng.*, 1982, **24**, 233–309.
28 H. Bluhm, M. Hävecker, A. Knop-Gericke, E. Kleimenov, R. Schlögl, D. Teschner, V. I. Bukhtiyarov, D. F. Ogletree and M. Salmeron, *J. Phys. Chem. B*, 2004, **108**, 14340–14347.
29 A. Knop-Gericke, M. Hävecker, T. Neisius and T. Schedel-Niedrig, *Nucl. Instrum. Methods Phys. Res., Sect. A*, 1998, **406**, 311–322.
30 A. Knop-Gericke, M. Hävecker, T. Schedel-Niedrig and R. Schlögl, *Top. Catal.*, 2000, **10**, 187–198.
31 S. Tanuma, C. J. Powell and D. R. Penn, *Surf. Interface Anal.*, 1994, **21**, 165–176.
32 J. J. Yeh and I. Lindau, *At. Data Nucl. Data Tables*, 1985, **32**, 1–155.
33 D. R. Penn, *J. Electron Spectrosc. Relat. Phenom.*, 1976, **9**, 29–40.
34 D. A. Shirley, *Phys. Rev. B: Solid State*, 1972, **5**, 4709–4714.
35 Y. Jin and A. K. Datye, *J. Catal.*, 2000, **196**, 8–17.
36 E. E. Unmuth, L. H. Schwartz and J. B. Butt, *J. Catal.*, 1980, **61**, 242–255.
37 U. R. Pillai and S. Deevi, *Appl. Catal., B*, 2006, **64**, 146–151.
38 M. D. Shroff and A. K. Datye, *Catal. Lett.*, 1996, **37**, 101–106.
39 J. J. Retief, *Powder Diffr.*, 1999, **14**, 130–132.
40 C. B. Finch, G. W. Clark and O. C. Kopp, *Am. Mineral.*, 1980, **65**, 381–389.
41 F. M. F. de Groot, M. Grioni, J. C. Fuggle, J. Ghijsen, G. A. Sawatzky and H. Petersen, *Phys. Rev. B: Condens. Matter*, 1989, **40**, 5715–5723.
42 P. A. van Aken, B. Liebscher and V. J. Styrsa, *Phys. Chem. Miner.*, 1998, **25**, 494–498.

43 M. Grioni, J. B. Goedkoop, R. Schoorl, F. M. F. de Groot, J. C. Fuggle, F. Schäfers, E. E. Koch, G. Rossi, J. M. Esteva and R. C. Karnatak, *Phys. Rev. B: Condens. Matter*, 1989, **39**, 1541–1545.
44 G. van der Laan, R. A. D. Pattrick, C. M. B. Henderson and D. J. Vaughan, *J. Phys. Chem. Solids*, 1992, **53**, 1185–1190.
45 F. M. F. de Groot and A. Kotani, *Core Level Spectroscopy of Solids*, Taylor & Francis, New York, 2008.
46 W. M. Heijboer, A. A. Battiston, A. Knop-Gericke, M. Havecker, R. Mayer, H. Bluhm, R. Schlögl, B. M. Weckhuysen, D. C. Koningsberger and F. M. F. de Groot, *J. Phys. Chem. B*, 2003, **107**, 13069–13075.
47 A. F. H. Wielers, A. J. H. M. Kock, C. E. C. A. Hop, J. W. Geus and A. M. van Der Kraan, *J. Catal.*, 1989, **117**, 1–18.
48 C. T. Chen, Y. U. Idzerda, H. J. Lin, N. V. Smith, G. Meigs, E. Chaban, G. H. Ho, E. Pellegrin and F. Sette, *Phys. Rev. Lett.*, 1995, **75**, 152.
49 J. J. Burton and E. S. Machlin, *Phys. Rev. Lett.*, 1976, **37**, 1433.
50 M. Hansen, *Constitution of Binary Alloys*, McGraw-Hill, New York, 1958.
51 G. Hollinger, *Appl. Surf. Sci.*, 1981, **8**, 318.
52 F. Karadas, G. Ertas and S. Suzer, *J. Phys. Chem. B*, 2004, **108**, 1515–1518.
53 H. P. Bonzel, G. Brodén and H. J. Krebs, *Appl. Surf. Sci.*, 1983, **16**, 373–394.
54 H. P. Bonzel and H. J. Krebs, *Surf. Sci.*, 1981, **109**, L527–531.
55 J. G. van Ommen, W. J. Bolink, J. Prasad and P. Mars, *J. Catal.*, 1975, **38**, 120–127.
56 C. S. Kuivila, P. C. Stair and J. B. Butt, *J. Catal.*, 1989, **118**, 299–311.
57 U. Lindner and H. Papp, *Appl. Surf. Sci.*, 1988, **32**, 75–92.
58 N. S. McIntyre and D. G. Zetaruk, *Anal. Chem.*, 1977, **49**, 1521–1529.
59 H. P. Bonzel and H. J. Krebs, *Surf. Sci.*, 1980, **91**, 499–513.
60 J. B. Butt, *Catal. Lett.*, 1990, **7**, 61–81.
61 D. J. Dwyer and J. H. Hardenbergh, *J. Catal.*, 1984, **87**, 66–76.
62 J. P. Reymond, P. Meriaudeau and S. J. Teichner, *J. Catal.*, 1982, **75**, 39–48.
63 M. E. Dry, T. Shingles, L. J. Boshoff and G. J. Oosthuizen, *J. Catal.*, 1969, **15**, 190–199.
64 N. Lohitharn and J. G. Goodwin Jr, *J. Catal.*, 2008, **260**, 7–16.
65 G. Brodén, G. Gafner and H. P. Bonzel, *Surf. Sci.*, 1979, **84**, 295–314.
66 D. C. Grenoble, M. M. Estadt and D. F. Ollis, *J. Catal.*, 1981, **67**, 90–102.

